Anne-Françoise Obaton,[1,2] Bryan Butsch,[3]
Stephen McDonough,[4] Ewen Carcreff,[5] Nans Laroche,[5]
Yves Gaillard,[6] Jared B. Tarr,[1] Patrick Bouvet,[6]
Rodolfo Cruz,[4] and Alkan Donmez[1]

Evaluation of Nondestructive Volumetric Testing Methods for Additively Manufactured Parts

Citation

A.-F. Obaton, B. Butsch, S. McDonough, E. Carcreff, N. Laroche, Y. Gaillard, J. B. Tarr, P. Bouvet, R. Cruz, and A. Donmez, "Evaluation of Nondestructive Volumetric Testing Methods for Additively Manufactured Parts," in *Structural Integrity of Additive Manufactured Parts*, ed. N. Shamsaei, S. Daniewicz, N. Hrabe, S. Beretta, J. Waller, and M. Seifi (West Conshohocken, PA: ASTM International, 2020), 51–91. http://doi.org/10.1520/STP162020180099[7]

ABSTRACT

Additive manufacturing enables the production of customized and complex parts. These two aspects are attractive for the aerospace and medical sectors. In these critical sectors, however, governed by strict safety requirements, the quality of the parts is of paramount importance, and the technology has advanced at a much faster pace than regulations and quality controls. The reliability of the parts must be guaranteed, and hence quality control is needed. Considering the complexity of additively manufactured part shapes, the inspection methods need to be nondestructive, three-dimensional, and volumetric. X-ray

Eqr{tkij v'd{'CUVO'Kpvgtpctkijvu'tgugtxgf·='Y gf'Lcp'3; '37-3: -57'I OV'4244
Fqy pqcf gf Irtkpvgf 'd{
WU0F GRV'QH'EQO O GTEG1PKV*WU0F GRV'QH'EQO O GTEG1PKV+'rwuwcpv'vq'Nkegpug'Ci tggo gpv0'Pq'hwtvgj gt'tgrtqf wevkqpu'cwj qtk| gf 0

computed tomography is presently the most appropriate method, but the relatively high cost and testing duration make routine inspection difficult. Thus, alternative nondestructive volumetric methods are required. In this paper, four alternative methods utilizing acoustic waves (resonant acoustic method, process compensated resonance testing) and ultrasonic waves (conventional ultrasonic testing, phased array ultrasonic testing combined with total focusing method) are investigated and compared with X-ray computed tomography using synchrotron radiation.

Keywords

nondestructive testing (NDT), volumetric NDT, additive manufacturing (AM), acoustic methods, ultrasound methods, X-ray computed tomography (XCT)

Introduction

One of the main advantages of additive manufacturing (AM) is to allow the fabrication of complex-shaped parts, including with inner cavities, that cannot be manufactured with conventional methods from a single block of material. Another main advantage of AM is the possibility to build customized parts for roughly the same price as some high-volume parts. These advantages are highly appreciated in the aerospace and medical sectors. But AM has been shown to produce specific types of defects in as-built parts, such as cross-layer defects, layer-specific defects, and unconsolidated or trapped powder defects. In these critical aerospace and medical sectors, the quality requirements of the parts are particularly severe, and the parts must be certified before they can be used in their intended application. This is a challenge for quality control of parts with such complex geometry and inner cavities, especially those with the high surface roughness levels typical of AM surfaces. The inspection methods not only must be nondestructive, volumetric to screen inner cavities, and appropriate for high roughness and complex shapes, but also inexpensive and fast for routine inspections. Among existing volumetric nondestructive testing (NDT) methods, X-ray tomography is presently the most appropriate method to inspect the inner features and defects of complex AM parts. X-ray tomography is expensive, however, and the scanning process takes a long time. In addition, the resulting scan files are large; thus, they are not easily viewable. So, even if X-ray tomography is recommended for first article inspection (FAI), it is not suitable for routine inspection of high-volume production of customized parts, for example. Alternative methods to X-ray tomography must be explored.[1,2]

All the NDT volumetric methods that currently are used for the characterization of conventionally manufactured parts require a new understanding of how they interact with AM parts. Then, further development of existing NDT methods, or novel ones, are greatly needed to handle the level of complexity that AM presents. The resonant acoustic and ultrasound NDT linear volumetric methods are potentially valuable techniques that need to be explored for AM parts.

This paper presents the capabilities of some of the existing acoustic and ultrasonic volumetric NDT methods to inspect AM parts with specific defects. The artifacts proposed by ISO TC261/ASTM F42 Joint Group 59 (JG59) "NDT for AM parts" are used in this study. The paper also presents results obtained with X-ray computed tomography (XCT) using synchrotron radiation as a comparison.

The paper is structured as follows: the first section is dedicated to the presentation of JG59 and their standards development regarding NDT inspections using a specially designed artifact. The second section describes the fabrication of this artifact in different materials, and the last section presents the principles, inspection results on the artifacts, and benefits and drawbacks of the following five volumetric NDT methods:

- whole-body inspection methods using acoustic waves: (1) resonant acoustic method (RAM) and (2) process compensated resonance testing (PCRT),
- selective inspection methods using ultrasonic waves: (3) conventional ultrasonic testing (CUT) and (4) phased array ultrasonic testing (PAUT) methods, and
- X-ray for comparison: (5) XCT using synchrotron radiation (SRXCT).

STANDARDIZATION GROUP ISO TC261-ASTM F42 ON AM: JOINT GROUP JG59 ON NDT FOR AM PARTS

Because AM is causing a revolution in manufacturing capabilities, many industries are interested in taking advantage of these methods. Each time a new technology grows in capability and use, however, standardization issues arise that must be overcome for the technology to continue its advancement. Several standards developing organizations (SDOs) are addressing this subject. The International Organization for Standardization (ISO) and ASTM International have implemented a formal agreement to codevelop a series of AM standards through several joint groups (JG). JG59 of ISO Technical Committee (TC) 261 and ASTM F42 is dedicated to NDT for AM parts.

Goal of the JG59

Several standards dedicated to NDT of manufactured parts already exist, and the JG59 does not aim to duplicate these standards. AM is different from other manufacturing processes like casting, forging, and machining. With AM, parts are built layer by layer from raw feedstock, such as metal powder, so one might say that the part is manufactured simultaneously with the material. This also means that the microstructure of the built material and the potential for embedded defects are specific to the AM technology. As mentioned previously, AM enables manufacturers to build complex geometries but with rough surfaces. Therefore, existing NDT methods must be evaluated for AM applicability. These methods might need to be adapted to accommodate AM characteristics.

Furthermore, new NDT methods also may be needed. Thus, a primary goal of the JG59 "NDT for AM parts" is to write a best practice guide presenting potential NDT methods suitable for post-process inspection of AM metallic parts, referring to existing NDT standards when appropriate. This best practice guide will contain a list of typical AM defects that can be found in two of the main types of metal additive manufacturing process categories used in industry: power bed fusion (PBF) and directed energy deposition (DED). It will give recommendations for NDT methods suitable for the special features of AM. The first version of this guide should be complete by the end of 2020.

To develop this guide, joint group members have designed and fabricated several artifacts with typical AM defects in different materials. These artifacts were then characterized by different NDT methods by the JG59 members (**table 1**) to evaluate the behaviors and potential for each NDT method for use with AM parts.

TABLE 1 NDT technologies investigated by JG59 with star artifacts in different materials

Material	NDT Technologies	Center/Company/University
Hastelloy X	X-Ray Computed Tomography (XCT)	MTC, UK
	Phased Array Ultrasonic Testing (PAUT)	University of Bristol, UK
	Process Compensated Resonance Testing (PCRT)	Vibrant, Germany
	Nonlinear acoustic method (NLA)	Theta Tech, UK
	Thermography testing (TT)	University of Bath, UK
	Digital Radiography testing (RT)	FujiFilm, USA
Maraging Steel	XCT	MTC, UK
	PAUT	University of Bristol, UK
	PCRT	Vibrant, Germany
	NLA	Theta Tech, UK
	TT	University of Bath, UK
	RT	FujiFilm, USA
Cobalt Chrome	Resonance Acoustic Method (RAM)	NIST/LNE and The Modal Shop, USA/France
	XCT	NIST/LNE, USA/France
	Synchrotron XCT (SRXCT)	Novitom, CTIF, LNE, France and NIST, USA
Stainless Steel	XCT	EWI, USA
	PAUT	EWI, USA
	XCT-Low Energy	ISS, Germany
	XCT	MTC, UK
	RAM	NIST/LNE and The Modal Shop, USA/France
	PCRT	NIST/LNE and Vibrant, USA/France

(continued)

TABLE 1 *(continued)*

Material	NDT Technologies	Center/Company/University
Aluminum	XCT	MTC, UK
	Conventional Ultrasonic Testing (CUT)	NIST/LNE and OKOS, USA/France
	PAUT–Total Focusing Method (TFM)	TPAC, LNE, France and AOS, NIST, USA
Titanium	XCT	MTC, UK
Titanium	SRXCT and Neutron diffraction ND	ESRF and ILL, France

## Star Artifact with Typical AM Defects

This artifact was designed by JG59 to be optimized for laboratory 450-kV XCT. The size of the artifact depends on the density of the material. It is in the shape of a star (**fig. 1**), hence, its name: star artifact. The artifact contains the following defects unique to AM parts:

- Cross-layer defects that are represented by vertical cylinders of different diameters but the same length (These cylinders are connected to each other and open to outside at the bottom of the star, so that powder is released at the largest diameter cylinder.)
- Layer-specific defects that are represented by horizontal cylinders of different diameters but the same length, with an open end to release powder
- Unconsolidated/trapped powder defects that are represented by spheres of different diameters and internal cylinders in various orientations

Voids and porosities are common defects also found in conventional manufacturing and are mostly covered by existing NDT standards.

These defects are located in critical areas such as deep sections and hard-to-reach areas, in five different regions. Two versions of the star design, designated as S1 and S2, were used in the evaluation of NDT methods (**fig. 1**). In these two

FIG. 1 Schematics of the AM star artifacts (design S1 and S2) proposed by JG59 (where *R* is a Region in the artifact, *h* and a define the height and width of the artifact, respectively, and numerical values are given in **table 2**).
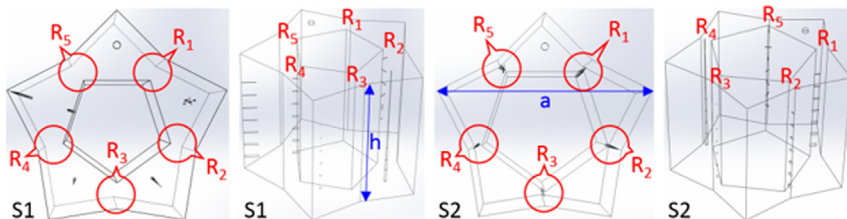
versions, the defects are of the same size, same height along the part, and the same orientation; the only difference is their locations. The S2 design has the defects in thinner sections of the star branches, whereas the S1 design has the defects in the thicker sections. All defects are in the range of 100 µm to 800 µm in diameter.

At NIST, we evaluated statistical NDT methods that required a large number of samples. Considering this fact, we decided to build half-size stars also. The sizes of the defects, however, remained the same.

STAR ARTIFACT FABRICATION

The star artifacts were manufactured by different members of the JG59, depending on their capabilities in terms of AM equipment and materials. NIST built star artifacts in cobalt-chromium (Co-Cr) (figs. 2A and 2B) and in stainless steel (SS) (figs. 2C and 2D) using AM machines belonging to the laser PBF process category. Zodiac Aerospace built aluminum star artifacts using also a laser PBF process. The characteristics of the manufactured star artifacts are shown in table 2 and a picture representing the finished star artifacts is shown in figure 3. Because some of the NDT methods investigated require statistical analysis, significantly more artifacts (specifically, SS artifacts) were built for those methods to establish the baseline for artifacts with no defects. Furthermore, to evaluate the capability of such techniques to sort parts based on the numbers of defects they contain, stars with different numbers of defects were manufactured in two similar builds (i.e., the same location on

FIG. 2   Photos of the manufacturing of the Co-Cr (*A* and *B*) and SS (*C* and *D*) star artifacts, during the build (*A* and *C*) and after the build on the machine platform (*B* and *D*).
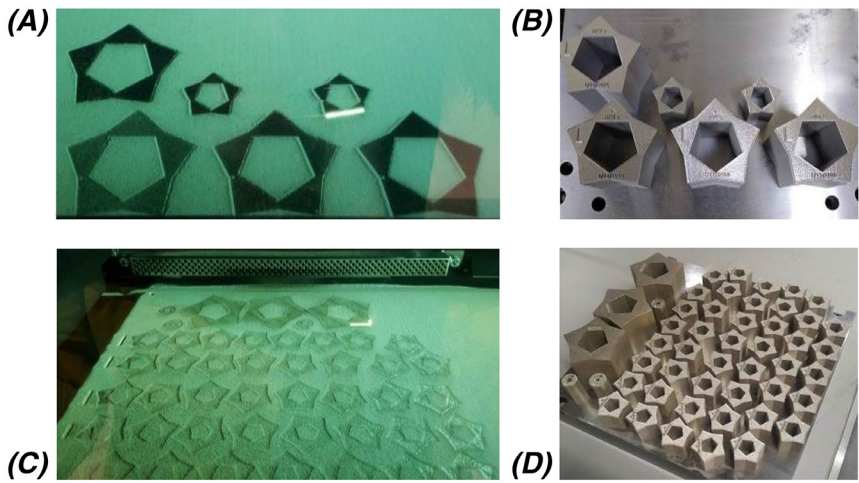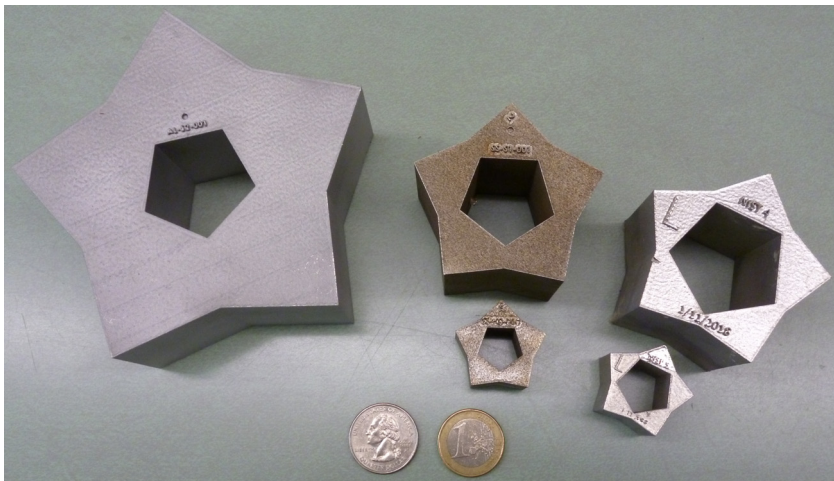
TABLE 2 Characteristics of the manufactured star artifacts

Material	Version	Size: full/half (HF)	Quantity
Cobalt-chrome-molybdenum-based superalloy Co-Cr MP1	S0	Full (a = 60 mm, h = 45 mm)	1
	S2		3
	S0	Half (size of defects/2 also (a = 30 mm, h = 22.5 mm)	1
	S2		1
Aluminum AlSi10Mg	S1	Full (a = 114 mm, h = 45 mm)	1
	S2		1
Stainless steel 17-4	S0	Full (a = 60 mm, h = 45 mm)	2
	S1		2
	S2		2
	S0	Half (a = 30 mm, h = 22.5 mm)	40
	S1		8
	S2		8
	S2	HF without defect in Region 1	8
	S2	HF without defect in Regions 1 and 2	8
	S2	HF without defect in Regions 1, 2, and 3	8
	S2	HF without defect in Regions 1, 2, 3, and 4	8

Note: S0 = a fully dense part, without inner features representing the defects; a = the width of the star; h = the height of the star; see **figure 1**.

FIG. 3 Photos of the manufactured star artifacts, from left to right: Al, SS, and Co-Cr.

Eqr {tki j v'd{ 'CUVO "Kpvt!"cm'tki j vu'tgugtxgf ±"Y gf 'Lcp"3; '37-3: -57'1 O V'4244
F qy pmqcf gf Ir tkpvgf 'd{
WUO'F GRV'QH'EQO O GTEG/P KUV'*WUO'F GRV'QH'EQO O GTEG/P KUV+'r wtuwcpv'vq 'Nlegpug'Ci tggo gpv0P q 'hwtyj gt 'tgrtqf wevkqpu'cwj qtk| gf 0

the AM build platform, with two or three marginally different parts added on the platform between the first and second build):

- eight similar parts with defects in the 5 Regions, such as defined by the JG59;
- eight similar parts with defects in only Region 1;
- eight similar parts with defects in only Regions 1 and 2;
- eight similar parts with defects in only Regions 1, 2, and 3; and
- eight similar parts with defects in only Regions 1, 2, 3, and 4.

Four of the eight stars are from one build, and the other four are from a second build.

VOLUMETRIC NDT METHODS EVALUATED

Nondestructive inspection methods can be separated into two main groups: (1) surface and subsurface methods enabling only a surface and subsurface inspection of the test object (e.g., by visual, dye penetrant, magnetic particles, eddy current, thermography for metal) and (2) volumetric methods enabling volumetric inspection of the test object (e.g., by ultrasound, radiography, thermography for polymer, acoustic emission, X-ray tomography).[3,4] Some volumetric methods, however, can be limited in terms of the inspectable thickness according to the material of the part tested. Volumetric methods also can be divided into two main groups: whole-body inspection methods and selective inspection methods. The whole-body inspection methods do not provide information about defect locations, whereas selective inspection methods do provide such information. We have investigated volumetric methods from both groups to evaluate their respective potential for inspecting AM parts.

Whole-Body Inspection Methods

Resonant Ultrasound Spectroscopy (RUS) Methods

Principle of RUS Methods—There are several variants of RUS methods, as described in ASTM E2001, *Standard Guide for Resonant Ultrasound Spectroscopy for Defect Detection in Both Metallic and Non-Metallic Parts,*[5] but their basic principles are similar. These whole-body inspection approaches compare the frequency spectrum of the mechanical resonances of a set of reference parts, known as "good parts," with the frequency spectrum of the mechanical resonances of the test parts. These are pass/fail assessments. Two similar objects will have similar resonant frequency spectra. A shift of the frequency peaks of a part, compared with the statistical variation from the similar good parts, will be the signature of a structural change of the part (e.g., changes in part geometry or material properties associated with the mass, stiffness, and damping).

A characterization using RUS methods includes several steps. The first step consists of a mechanical impulse of the test object to make it vibrate as free as possible. Under this excitation, the object vibrates at its natural resonant frequencies. At the second step, the response of the test object is monitored by a sensor, and the

frequency spectrum is recorded. At the third step, this spectrum is compared with the spectrum of the good parts, which are obtained following the same first two steps. For this comparison, the well-defined resonant peaks for each good part are identified. A subset of such resonant peaks that are consistent for all reference parts peaks and have distinct separation with bad parts are selected for further consideration. The ranges (boundaries) in variations in each resonant peak frequency of the good parts are evaluated, these are called "criteria." Outliers of these variations must be excluded from these ranges. The measured resonant peak frequencies of the test parts are compared against the corresponding ranges in frequencies of the good parts. All test parts with frequency peaks outside of these boundaries are rejected as faulty parts.

RAM[6] and PCRT, described in ASTM E2534, *Standard Practice for Process Compensated Resonance Testing via Swept Sine Input for Metallic and Non-Metallic Parts*,[7] are two types of RUS methods.

Principles of RAM—In the RAM, the excitation is done by an impact hammer (first step) and the resulting acoustic frequency data are obtained with a microphone. No contact probes need to interact with the test part. This allows the parts to resonate in as free a state as possible. The output of the microphone is converted into a frequency spectrum using a high-speed analog-to-digital converter (24 bits) performing a fast Fourier transform to determine resonant peaks (second step). Finally, a statistical analysis conducted with software reveals whether or not the test parts fall within the defined criteria (third step). If at least one of the measured resonant peak frequencies of the test part lays outside of the established frequency ranges of the good part, the test part is considered bad. For a part to pass RAM testing, it must pass every individual criteria point. For a part to fail RAM testing, it needs to fail only one criteria point.

RAM Inspection of the SS Half-Size Star Artifacts—**Figure 4** shows the setup used for the RAM measurements[8] of eighty-eight SS half-size stars (**fig. 5**), resulting from the

FIG. 4   (*A*) The Modal Shop RAM set-up (*A*) and (*B*) inspection of the half-size SS star artifacts using the set-up with the automatic hammer.

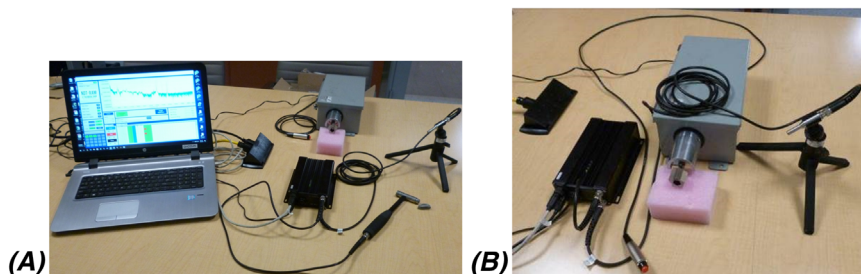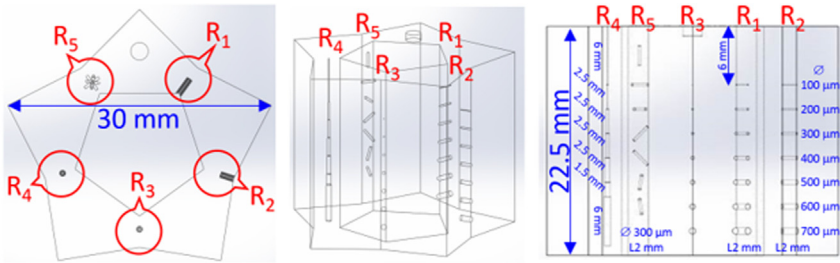Eqr{tki j v'd{ 'CUVO "Kp{ri'%'cnltki j w't gugtxgf +='Y gf 'Lcp"3; '37:3: -57'1 O V'4244
F qy pmqcf gf Irtkpxgf "d{
WU0F GRV'QH'EQO O GTEG/P KUV'*WU0F GRV'QH'EQO O GTEG/P KUV+'r wtuwcpv'vq 'Nkegpug'Ci tggo gpv0P q 'hwtvj gt'tgrtqf wevkqpu'cwj qtk| gf 0

two successive builds (table 2). Among them, 20 from each build were manufactured with no defects and were considered as reference parts to define the baseline for the criteria. The stars were systematically weighed before the test as the inspection software enables weight compensation. Then, the star artifacts were hit with an automatic hammer on the sides of their bottom faces, as these positions were experimentally found to provide the least amount of damping. To determine optimum impact positions, a part was hit in several different positions and orientations. The impact location and orientation resulting in the greatest signal-to-noise ratio of the resonant peaks as well as the greatest frequency separation between good and bad parts was selected as the optimum position and orientation for the subsequent tests.

When performing the tests, each part was hit three consecutive times at three different branches of the star at the base. This procedure allowed us to check for repeatability and reproducibility. For consistent impacts on every part, the same positions on the same branches of the stars were always struck. The frequency window considered for analysis ranged from 500 Hz to 50 kHz, and a resolution of 3.5 Hz was chosen, which gives an acquisition time of 0.23 s.

We considered the first and second build separately. The data on the 20 reference parts were first gathered, and then the remaining 24 stars with defects were tested. The tests were repeated on two consecutive days. The acceptance criteria to define the baseline for comparison of the resonant peaks, from this first set of data, were set up over six frequency bands, as shown in figure 6. This figure shows the complete spectrum for a single part test. The vertical lines labelled 1 to 6 show the bands of the resonant peaks chosen for evaluation. These criteria are used by the software to sort the bad parts from the good. The data for a part must pass all the criteria to pass resonance testing.

There is a constant shift, for all peaks, in the frequency spectrum between build 1 and build 2 (table 3). The same criteria (same width), however, could be chosen between build 1 and build 2. It is common (especially in a powder metal build process) to see small shifts in resonant spectra from build to build because of variations

FIG. 6 Typical half-size SS star artifact RAM spectrum showing the subset of the six resonant peaks used for comparison criteria.

TABLE 3 RAM criteria, center frequencies, and shift between build 1 and build 2 for the half-size SS star artifacts

	Center Frequency		Frequency Shift (Hz)
	Build 1 (Hz)	Build 2 (Hz)	
Criterion 1	27,742.5	27,549.5	−193
Criterion 2	28,072.5	28,017.5	−55
Criterion 3	31,489.5	31,455	−34.5
Criterion 4	34,027.5	34,001	−26.5
Criterion 5	34,489	34,601	112
Criterion 6	39,401	39,366.5	−34.5

in the raw material, manufacturing conditions, and environmental conditions. Note that the general shape of the frequency spectrum does not change from build to build, just a constant shift in frequency is observed, which is based on changes to the mass or stiffness of the parts. Also note that the spectrum shift is a global shift for the entire build and does not affect the ability to sort the good parts from the defective parts.

The outcome of the resonant acoustic test for the eighty-eight SS half-size star artifacts is displayed in **table 4**.

TABLE 4 RAM overall pass/fail results for the 88 half-size SS star artifacts

	Build 1		Build 2	
	Pass	Fail	Pass	Fail
Good parts	20	0	19	1
Bad parts with defects	0	24	0	24

FIG. 7 Half-size SS star artifact RAM spectra of a reference part in grey and of a part with defects in black.
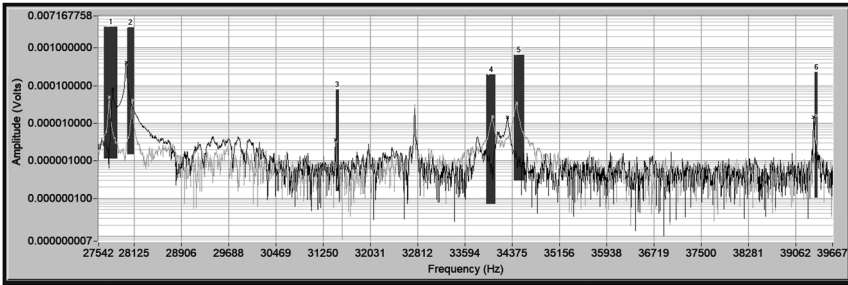
We defined criteria that allowed us to differentiate the good parts from parts with internal defects. The reference parts showed a significant difference in resonance compared with the parts with defects (fig. 7). One reference part out of 20 was rejected, however, as its resonance peaks were too different from the other reference parts. This is probably due to an unintentional organic defect in that part resulting from small variations in the manufacturing process. In the range of frequencies analyzed, the parts could not be sorted based on the number of defects they contain.

The main benefits of RAM are as follows:

- easy to use
- fast
- simple
- no restriction in size
- no restriction in shape
- no roughness restriction
- no part preparation or fixturing required
- suitable for medium to high volumes
- able to identify defective parts
- suitable for production end of line testing or routine quality inspection

The main drawback of the method is that it is not possible to identify the type or location of defects in the part.
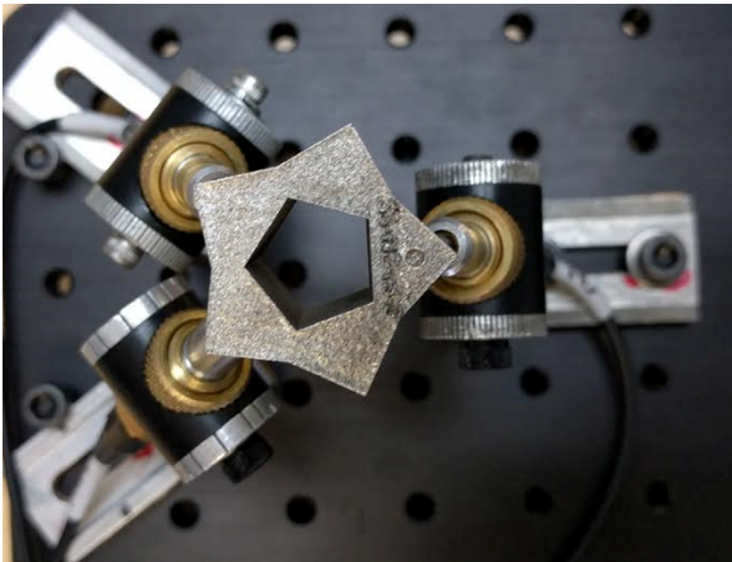
PCRT

Principle of PCRT—PCRT[7] uses piezoelectric transducers in contact with the part, but otherwise is similar to RAM. Excitation of the part uses a piezoelectric transducer to generate a low-energy swept-sine wave, generally with ultrasonic frequencies (5 kHz to 500 kHz). Then the frequency response is recorded with other piezoelectric transducers. Each test requires configuring a specific fixture and optimizing data collection settings for each new part geometry.

The PCRT system used to characterize the star artifacts is fully automated with one transmitter and two receiver transducers. For data analysis, the system uses a Z-score (ASTM E3081, *Standard Practice for Outlier Screening Using Process Compensated Resonance Testing via Swept Sine Input for Metallic and Non-Metallic Parts*)[9] to identify outliers of resonance peak variations within a population of parts. In addition, when a simple resonance analysis is insufficient due to the interlacing of the spectra for good and bad parts, the system uses a pattern recognition tool, such as the Mahalanobis-Taguchi system (MTS)[10] to sort the parts.

PCRT Inspection of the SS Half-Size Star Artifacts—Figure 8 shows the setup used for the PCRT inspection of 74 of the 88 SS half-size stars resulting from the two successive builds (table 2). We considered 20 and 18 parts as reference parts from builds 1 and 2, respectively. For each part, data were collected between 25 kHz and 225 kHz in less than 1 min and then processed using Z-score and MTS analysis. The tests scanned six resonant peaks (60 Hz, 70 Hz, 110 Hz, 116 Hz, 132 Hz, 180 Hz) and the calculations are based on those six frequencies. The data collection settings and scoring criteria were identical for both builds in the sample population.

The repeatability of resonance measurements was evaluated using one reference part, with more than 30 repetitions. The variations, expressed as the standard deviations, in each measured peak frequency with more than 30 repetitions were calculated. The frequency peaks with large variations were eliminated from the set of peaks to be

FIG. 8 PCRT set-up used for inspection of the half-size SS star artifacts.

Eqr{tki j v'd{'CUVO "Kpv\u'cph'tki j v'tgugtxgf +='Y gf 'Lcp'3; '37:3: -57'I O V'4244
F qy pncf gf 1tkpvgf 'd{
WUU'F GRV'QH'EQO O GTEG P KUV'*WUU'F GRV'QH'EQO O GTEG P KUV+'r wtuwcpv'vq 'Nkegpug'Ci tggo gpv0P q 'hwtvj gt 'tgrtqf wevkqpu'cwj qtk\gf 0

used for the defect detection criteria. The standard deviations for the remaining 26 resonant peaks were between 0.05% and 0.013% of the mean peak frequencies.

PCRT partial spectra for four good and four bad parts are compared in **figure 9**, which shows that the shift in frequency between good and bad parts is not the same for every resonant peak. To deal with this, a proprietary pattern recognition algorithm (Vibrational Pattern Recognition[11]) is used to differentiate the parts with defects from the parts with no defects. To confirm repeatability, these tests were run three times. Each test run gave the same results. The overall results are presented in **table 5**. As with RAM, we were able to sort the good parts from the ones with internal defects. The parts, however, could not be sorted by the number of defects they contain.

The main benefits of PCRT are as follows:

- fast
- no restriction in size
- no restriction in shape
- no roughness restriction

FIG. 9   Typical half-size SS star artifact PCRT spectrum. The four plots at the top represent four good parts and the four at the bottom represent four bad parts.
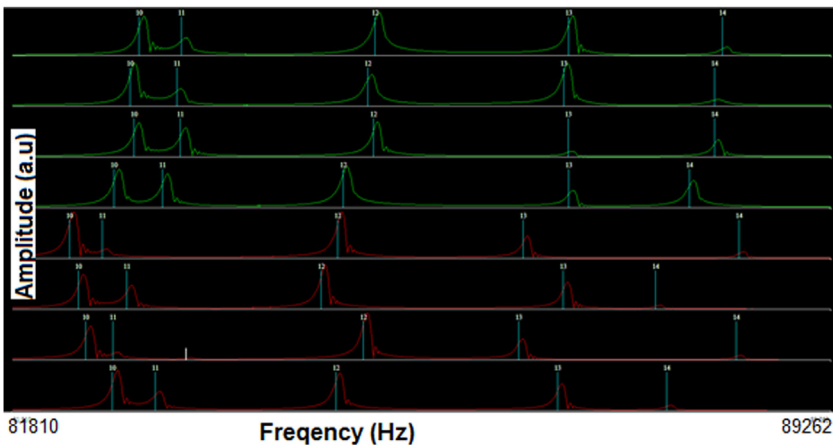

TABLE 5   PCRT overall pass/fail results for the 74 half-size SS star artifacts

	Build 1		Build 2	
	Pass	Fail	Pass	Fail
Good parts	18	0	20	0
Bad parts with defects	0	24	0	12

- suitable for medium to high volume
- able to identify defective parts
- suitable for production end of line testing, or routine quality inspection

The main drawbacks of PCRT are as follows:

- part set-up required
- not possible to identify the type or location of defects in the part

Selective Inspection Methods

Selective inspection methods use scanning techniques to inspect only selected regions of a part, possibly from multiple directions.

CUT

Principle of CUT—CUT, as described in ASTM E1001, *Standard Practice for Detection and Evaluation of Discontinuities by the Immersed Pulse-Echo Ultrasonic Method Using Longitudinal Waves,*[12] and explained by Olympus,[13,14] generally uses one or more piezoelectric transducers, which can act as a transmitter, receiver, or both, to produce ultrasound into the test part. The emitting frequencies are theoretically ranging from 20 kHz upward to 1 GHz, depending on the density of the material and on the size of the smallest defect to be detected. The ultrasound wavelength ($\lambda = v/f$, where v is the velocity of sound in the material of the tested part and f is the sound frequency) must be roughly the size of the smallest defect. Decreasing the wavelength allows the detection of smaller defects but reduces the penetration depth because attenuation increases significantly. When the CUT is performed in contact mode, the thin film of a couplant must be spread on the surface of the transducer to increase the transmission of the ultrasonic waves into the part. This eliminates variations due to microscopic air pockets, which greatly impede ultrasound. The acoustic impedance of the couplant should be similar to that of the test part. CUT, however, also can be performed in the noncontact mode. In that case, the transducer and part are immersed in a tank of liquid (generally water), which also serves as the couplant. This allows the ultrasound beam to be scanned over various regions of a part with minimal variations in the coupling.

When sound waves transmitted into the part, reflection, transmission, or refraction occurs at each boundary separating a defect from the surrounding material, and at the boundaries defining the part itself. The resultant echoes are detected by a transducer and processed to determine the presence of the defects and their approximate locations. The detailed scanning procedure and signal processing must compensate for confounding phenomena, such as mode conversion, scattering, and shadowing. These phenomena can prevent observation of some defects.

There are three possible ways of presenting the information (fig. 10):

1. A-scan (*x*-axis: *time, y*-axis: *reflected wave amplitude*): shows peaks on a graph (oscilloscope). The graph represents the amplitude of the reflected sound wave as a function of time. Position on the *x*-axis reflects the depth of

FIG. 10   Schematic representation of A, B, and C scans used in ultrasound inspection.
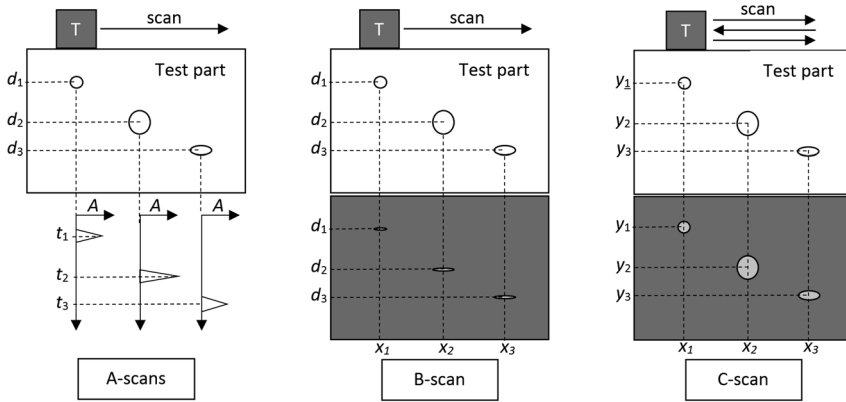
each reflecting feature or flaw. Position on the *y*-axis reflects the amplitude of the echo from each reflecting feature or flaw.

2. B-scan (*x*-axis: *linear position of the transducer, y*-axis: *depth of the reflector*, grey levels or colors: *reflected wave amplitude*): shows an image with different grey levels or colors corresponding to the amplitude of the reflection from each reflecting feature or flaw. Position on the *x*-axis shows the position of the transducer along its scan path. Position on the *y*-axis reflects the depth of each reflecting feature or flaw.

3. C-scan (*x*-axis: *linear position of the transducer on the x-axis, y*-axis: *linear position of the transducer on the y-axis*, grey levels or colors: *reflected wave amplitude, time of flight or depth*): shows an image viewed from the top (planar view) of a region of interest within the volume of the test specimen. The images display different grey levels or colors corresponding to the amplitude, time of flight, or depth of the signal for different positions of the transducer scanning the surface of the part. A C-scan image is formed in a plane normal to a B-scan image.

The CUT system used to inspect the star artifacts is associated with a software system (ODIS from OKOS), including amplitude, time domain, and frequency domain, and imaging in a real-time or post-collection review. The software enables simultaneous A-B-C-scan collection. The color code on the images indicates the amplitude of the signal (i.e., change in attenuation) such as displayed in **figure 11**, where black (in the center) corresponds to low amplitude and white (on the borders) to high amplitude.

CUT Inspection of the Aluminum S1 Star Artifact—The computer-aided design (CAD) of the S1 aluminum star artifact is shown in **figure 12**. This part was tested in

FIG. 11   Color code or grey code on the C-scan images (black in the center: low
amplitudes, white on the borders: large amplitudes).

the configuration shown in **figure 13**. One transducer, acting as a transmitter or receiver, was used with the artifact immersed in water. The part was first scanned from the top, and then from each side of its branches (**fig. 14**) using the longitudinal waves. The schematics of the scanning strategies are shown in **figure 14**. The characteristics of the transducer used for both scans are displayed in **table 6**. The respective water path distances between the transducer and the test artifact during the scan were 132 mm for the top surface scan, and 83 mm for the side surface scans. The gain was adjusted to 39 dB to obtain the 100% threshold reflection of the back wall of the star artifact. Then, to outline the important features inside the artifact, two time-domain windows (data 1 and data 2) were defined on the A-scan, such as the one shown in **figure 15**. These windows

FIG. 12   CAD of the aluminum star artifact, design S1, seen from different sides
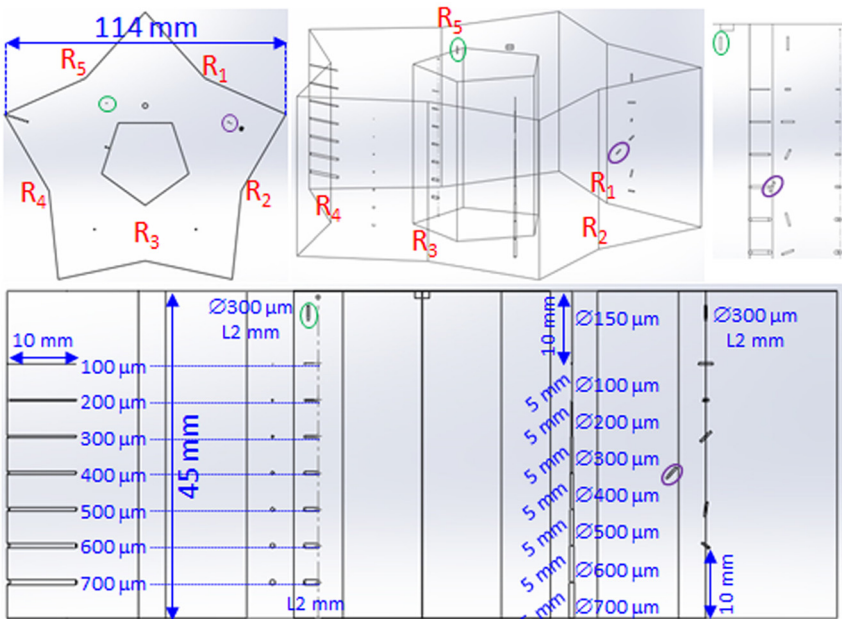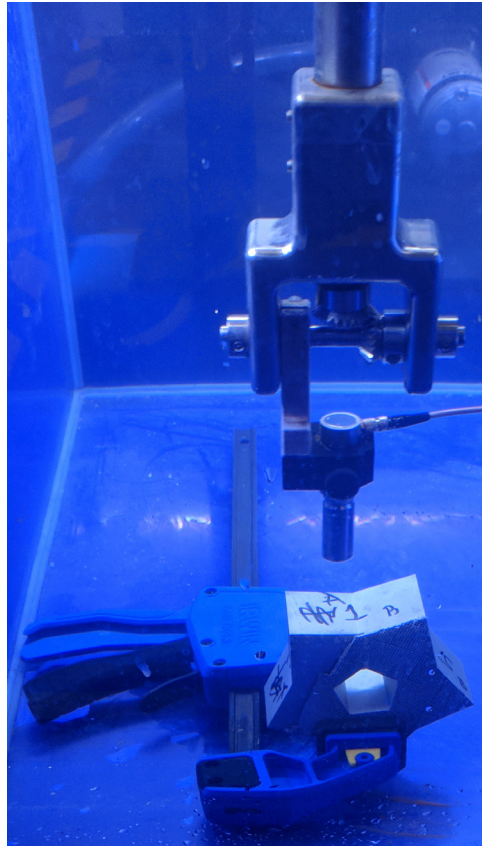(*R* refers to the Region in the star).

correspond to two different regions (depths) of interest in the artifact. Their widths (with corresponding ranges of depths) were determined based on the speed of sound in the material. The speed of sound given in the literature for wrought aluminum was chosen (as 6375 m/s). This value, however, might be different in layer-by-layer manufactured aluminum. Consequently, the uncertainty on the corresponding depths of interest is not negligible. Data 1, the longer rectangle on **figure 16**, excludes the top and rear surfaces of the part, whereas data 2, the shorter rectangle on **figure 16**, selects the region around the rear surfaces. The C-scan images shown in **figure 16** through **figure 20** are based on these two time-domain windows focusing on two different regions of depth.

Because all of the defects in the artifact are in the same position along its height, the first defect does not allow the rest of the defects to be inspected by CUT from the top surface of the star. In contrast, the C-scan images recorded from the side

FIG. 14 Scanning strategies of the aluminum star artifact using the CUT method.

Top scan   Side scan

TABLE 6 Transducer characteristics and experimental parameters used for the CUT inspection of the aluminum artifact

Scan	Type	Frequency (MHz)	Focal legnth (mm)	Diameter (mm)	Wavelength (mm)	Spot size (mm)	Resolution (mm)
		γ	f	Ø	$\lambda = \nu_{s/\gamma}$	$1.22 \times f/$ Ø$\times\lambda$	0.707×1.22 $f/$Ø$\times\lambda$
from top	Ceramic	25	6	9.5	0.3	0.2	0.1
from side	Ceramic	10	75	9.5	0.6	6.1	4.3
	Sound velocity in aluminum (mm/μs)		ν_s	6.4			

surfaces of the star artifact and presented in **figure 16** through **figure 20** reveal more information:

- The cylinders with different orientations (d_{12}, between Regions 1 and 2) cannot be observed in near field from sides labeled 1A and 2B on **figure 16**, probably because the gain was constant with distance. The larger ones can be seen in the far field from the side labeled 3B (**fig. 17**), but not from the side labeled 5A (**fig. 20**).
- The vertical cylinders with different diameters (d_{23}, between Regions 2 and 3) cannot be seen from the side labeled 1A (**fig. 16**) because the cylinders with different orientations (d_{12}) hide them. The larger cylinders can be seen from all sides, in near and far fields.

FIG. 15   Time-domain windows (rectangles) defined on the A-scan plot of the reflected
signal for data analysis of CUT.
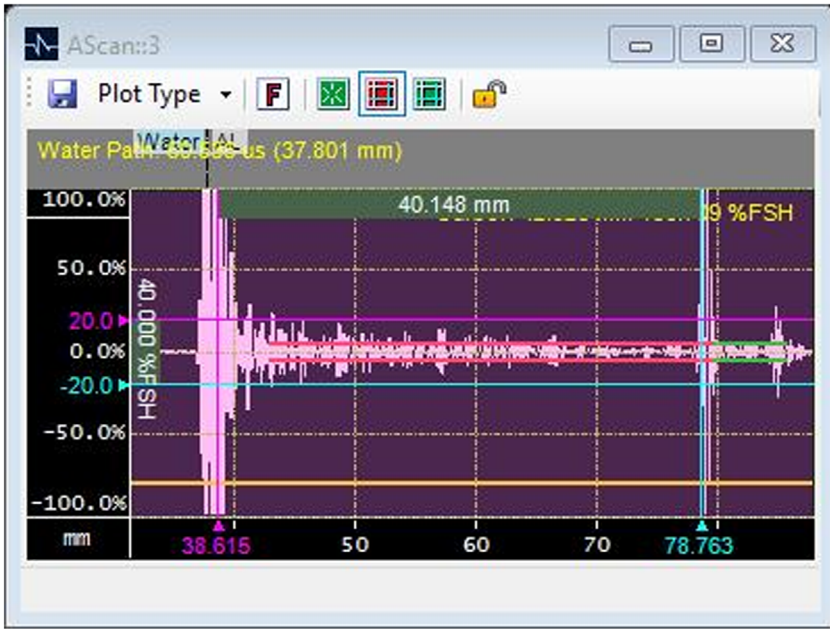
- The spheres of different diameters (d_{34}, between Regions 3 and 4) cannot be seen from any sides because the sphere shape is too complex to detect with ultrasound waves. Indeed, this geometry scatters the waves in every direction. Furthermore, these spheres are full of powder. Thus, the reflected wave reaching the transducer is very low in energy. In this experiment, the energy of the reflected wave might be too low to be detected. Although the spheres probably could have been detected with shear wave methodology, only longitudinal wave imaging was used during the present evaluation.

- The horizontal cylinders of different diameters located on an outside edge of the star (d_{45out}, between Regions 4 and 5) are not seen from most sides. This is probably due to the fact that they are positioned right at the borders of the time windows. So, because the widths of these windows are not accurate, they might be outside. They can all be seen and discretized, however, in the far field from the side labeled 3A (fig. 18). They appear right in the middle of the image rather than on an edge probably because of diffraction at the R4 edge of the star.

- The horizontal cylinders of different diameters located on an inside edge of the star (d_{45in}, between Regions 4 and 5) are not seen from most sides
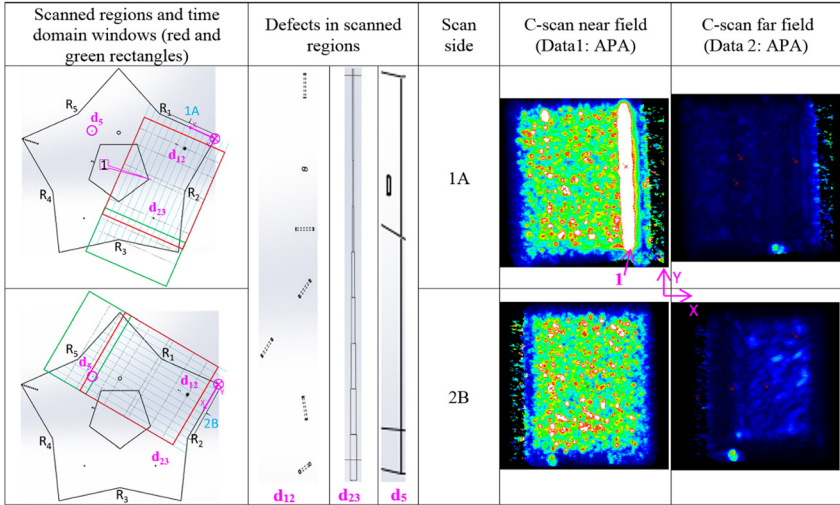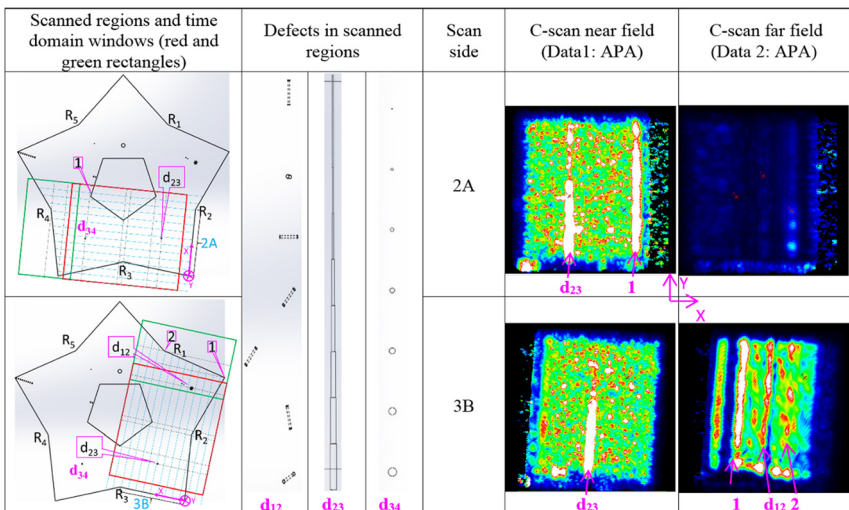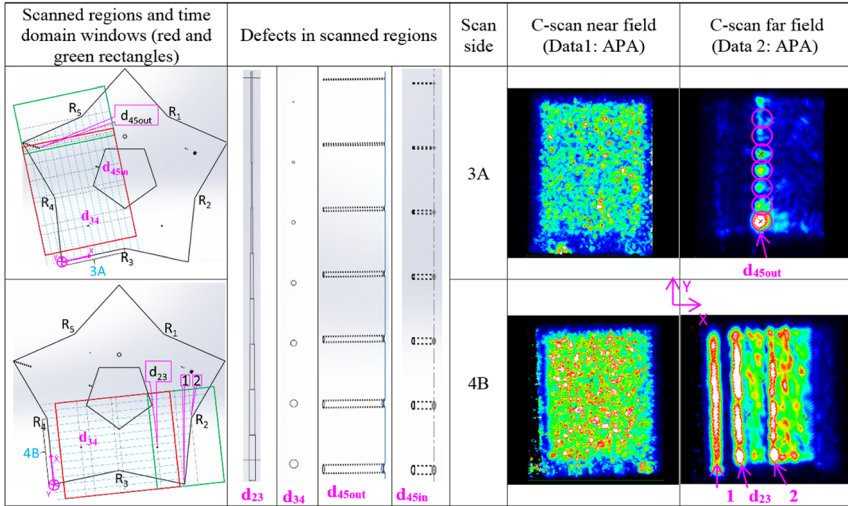
FIG. 16 CUT inspection from sides 1A and 2B of the aluminum star artifact. The parallel lines represent the longitudinal waves propagating from sides 1A/2B, "data" refers to the time domain window, and "APA" stands for "Absolute Peak Amplitude."

FIG. 17 CUT inspection from sides 2A and 3B of the aluminum star artifact. The parallel lines represent the longitudinal waves propagating from sides 2A/3B, "data" refers to the time domain window, and "APA" stands for "Absolute Peak Amplitude."

Eqr{tkij v'd{'CUVO "Kpvnï*cmïtkij w'tgugtxgf ±"Y gf 'Lcp"3; '37-3: -57'1 O V'4244
Fqy pmqcf gf Ir tkpvgf 'd{
WL0'F GRV'QH'EQO O GTEG/P KUV'*WL0'F GRV'QH'EQO O GTEG/P KUV+'r wtuwcpv'q 'Nkegpug 'Ci tggo gpv0P q 'hwtvj gt 'tgr tqf wevkqpu'cwij qtk|gf 0

probably because they are very small (2 mm long) and located on an edge. The larger ones, however, can be seen from the side labeled A4 (fig. 19) in the near field.

- There was a mistake in the CAD data used to manufacture the aluminum S1 star artifacts. One of the cylinders with a different orientation is isolated from the others (d_5 in Region 5, fig. 20). We might see it from the side labeled 1B (fig. 20) in the near field. The reason it cannot be seen from the other sides is probably due to its orientation.

Except for the spheres, all other types of larger defects were detected from at least one side, although they were not discretized in size. The interpretation of the image, however, is not straightforward and requires experience. In addition, the defects and their localization were known in advance. In the case of blind inspection, the analysis would have been even more difficult. Furthermore, the spatial resolution of the images, in that case, is not high enough to perform accurate dimensional measurements of the defects even though the standard object would have been used for comparison. Despite the surface roughness of the AM parts, we were able to scan the star artifacts from as-built surfaces, even from side surfaces, which generally are rougher than the top surfaces in AM. So, the roughness of the surface did not preclude CUT. Moreover, note that the size and thickness of the aluminum star do not allow for inspection with laboratory 225-kV XCT. Laboratory

FIG. 19 CUT inspection from sides 4A and 5B of the aluminum star artifact. The parallel lines represent the longitudinal waves propagating from sides 4A/5B, "data" refers to the time domain window, and "APA" stands for "Absolute Peak Amplitude."

FIG. 20 CUT inspection from sides 5A and 1B of the aluminum star artifact. The parallel lines represent the longitudinal waves propagating from sides 5A/1B, "data" refers to the time domain window, and "APA" stands for "Absolute Peak Amplitude."

450-kV XCT is required. This underlines an advantage of UT methods for large parts—that is, 450-kV XCT systems are relatively rare.

The main benefits of the CUT method are as follows:
- few roughness restrictions
- real-time imaging
- less restriction in size than XCT
- ability to identify the type and location of defects in the part

The main drawbacks of the CUT method are as follows:
- part set-up required
- experience required
- shape restriction
- not suitable for high volume and routine quality control
- no real discretization in size

PAUT

Principle of PAUT—The principle of PAUT is similar to that of CUT.[15] Instead of consisting of a single piezoelectric transducer, however, the PAUT probe is composed of an array of piezoelectric transducers. Each transducer of this array can be pulsed independently with respect to the others to generate several waves that will interfere. The waves that are in phase will be added together (constructive interference), whereas the ones that are out of phase will cancel each other (destructive interference). This results in a unique wavefront constituting a synthesized focused beam that can be oriented (controllable angle), shaped (controllable focal distance and focal spot size), and swept electronically. Dynamic control of the beam enables examining the complex shapes across a range of different perspectives without moving the probe. The spatial resolution of the images is linked to the number of elements in the array. The larger the number of elements, the better the resolution.

It is possible to improve the performance of the above-mentioned standard PAUT system by implementing a data acquisition method called full matrix capture (FMC) with a post-processing reconstruction algorithm known as total focusing method (TFM).[16–18] In the generic FMC acquisition method, a single transducer of the array is pulsed and the time domain signals (A-scans) are captured by all transducers in the array and stored for later processing. This is done for all transducers of the array. The number of data sets acquired is the square of the number of transducers. Thus, a 128-transducer probe will produce 16,384 raw A-scans. The offline data processing uses the complete set of time-domain data from all combinations of transmitting and receiving transducers. The reconstructed image from the A-scans is equivalent to making coherent summations over all transducers to focus at each point in the target region. Thus, FMC combined with TFM enables offline reconstruction of a more detailed image (with better spatial resolution, perspective, and defect definition) than a standard PAUT imaging method in which all array elements create a unique wavefront to form a beam with a fixed focus.

The instrument[19] that was used to perform the PAUT of the star artifacts implements both FMC and TFM. It also permits the acquisition of standard PAUT data. The software associated with the hardware enables simultaneous A-B-C-scan displays as well as a D-scan, which is similar to the C-scan but in a perpendicular direction. If the C-scan displays an image in the plane (XY), then the D-scan will display the image in the orthogonal plane (ZY). During the translation of the PAUT probe, the beam inside the probe is swept in the perpendicular direction to scan the entire surface. The color code or grey variations on the images is the same as the one described earlier for the CUT images (fig. 11).

PAUT–TFM of the Aluminum S1 and S2 Star Artifacts—Both of the S1 and S2 designs of the aluminum star artifacts, with the corresponding CAD shown in figures 12 and 21, could be tested using PAUT-TFM. Only one linear probe acting as a transmitter or receiver was used to induce the longitudinal waves. The probe is 32 mm long and composed of 128 transducers separated from each other by 0.25 mm (center to center). The star artifact, immersed in a tank of water for the coupling (fig. 22), was scanned only from one side of its branches (fig. 22), from the top to

FIG. 21   CAD of the aluminum star artifact, design S2, seen from different sides (R refers to the Region in the star).
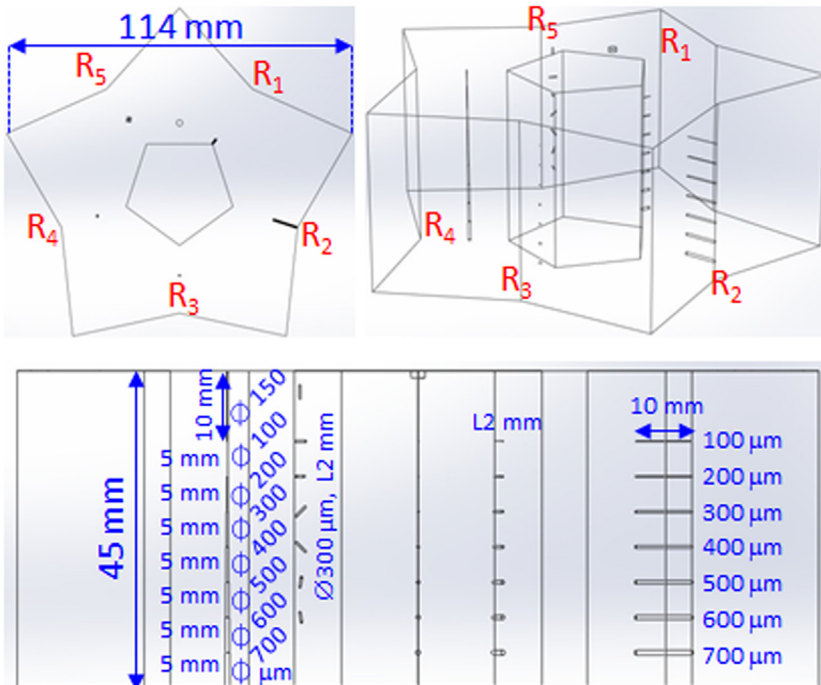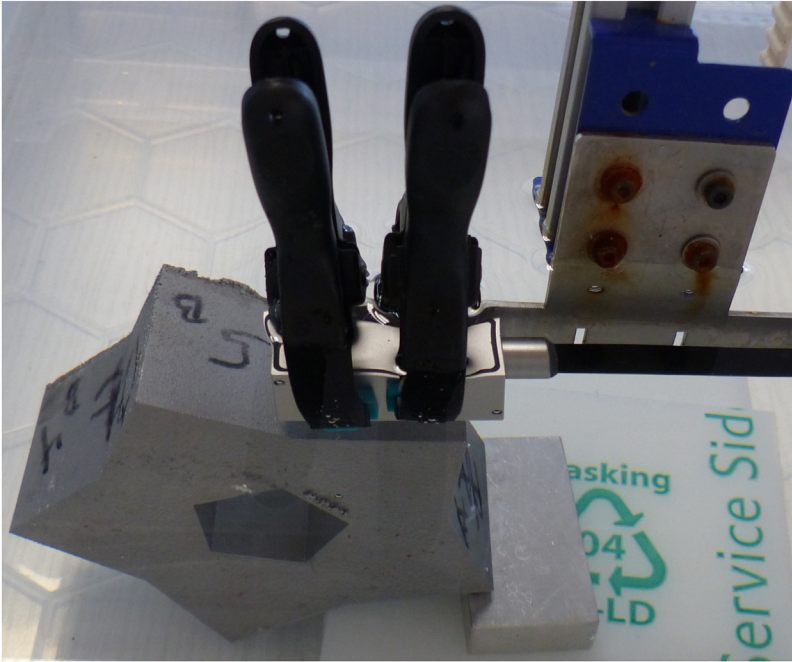
FIG. 22   PAUT-TFM side inspection of the aluminum star.

the bottom of the star (*y*-axis; i.e., sideways as shown in fig. 23). The transducers were operated at a center frequency of 10 MHz (bandwidth of 6 MHz), which corresponds to a wavelength of 0.62 mm in aluminum. The water path distance between the probe and the scanned surface of the artifact during the scan was 12.5 mm. Finally, the analog gain was set manually to 40 dB to properly visualize all of the defects and to acquire the data. The digital gain can be subsequently adjusted on the reconstructed image (300 pixels × 400 pixels) offline.

The A-, B-, C-, and D-scan presented in figure 23 through figure 27 for the S1 design and in figure 28 through figure 32 for the S2 design show interesting results:

- Three of the cylinders with different orientations can be seen from side 1A (fig. 23). The orientations of the other cylinders prevent detection.
- Five vertical cylinders with different diameters can be detected from side 2A (fig. 24) using the three optimized digital gains chosen to display the images. The cylinders with smaller diameters, down to 100 µm, can be detected with increased gain (fig. 24 bottom images) at the expense of the reduced quality of the image (lower signal to noise ratio).
- Three of the spheres of different diameters can be seen from side 3A (fig. 25).

FIG. 23   PAUT-TFM inspection from side 1A of the S1 aluminum star artifact. The parallel lines represent the longitudinal waves propagating from side 1A.
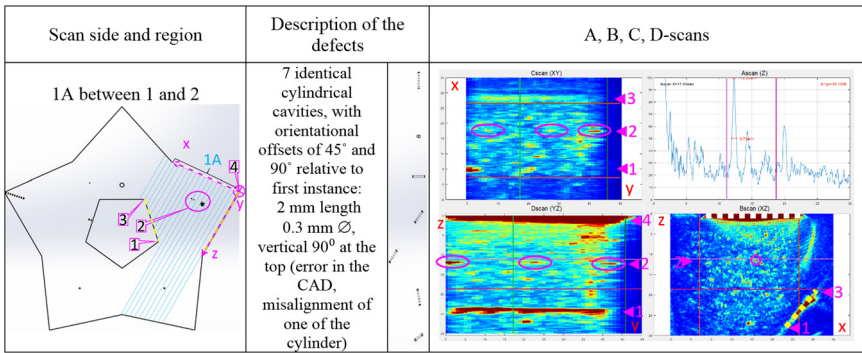

FIG. 24   PAUT-TFM inspection from side 2A of the S1 aluminum star artifact. The parallel lines represent the longitudinal waves propagating from side 2A. The two bottom scans correspond to higher digital gains.
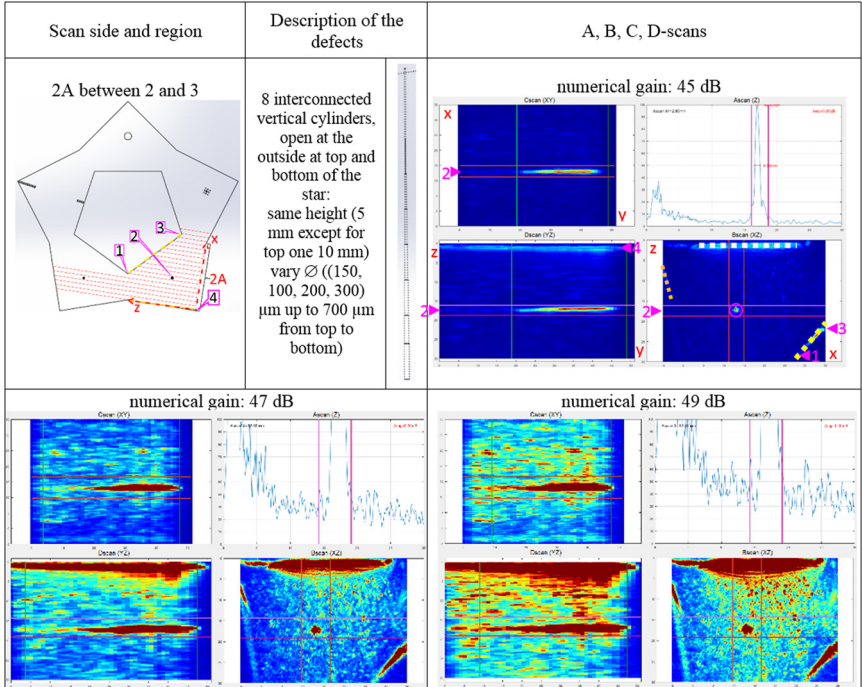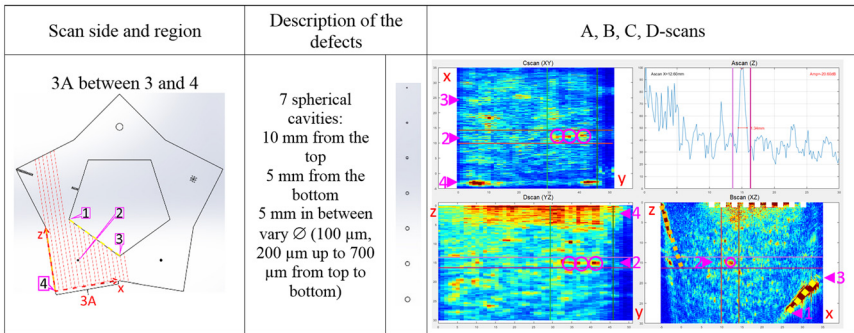
FIG. 25   PAUT-TFM inspection from side 3A of the S1 aluminum star artifact. The parallel lines represent the longitudinal waves propagating from side 3A.

Scan side and region	Description of the defects	A, B, C, D-scans
3A between 3 and 4	7 spherical cavities: 10 mm from the top 5 mm from the bottom 5 mm in between vary ∅ (100 μm, 200 μm up to 700 μm from top to bottom)	

- Three of the horizontal cylinders of different diameters (10 mm long) located on an outside edge of the star can be seen from side 4A (**fig. 26**). Their position on the edge hides the others.
- Some horizontal cylinders of different diameters located on an inside edge of the star are seen from side 4A (**fig. 27**). They are located on an edge and are short (2 mm long), so they are difficult to differentiate from the reflection of the edge.
- It does not seem that we can see the single cylinder manufactured by mistake.

The defects are more visible on PAUT-TFM images from the S2 design than from the S1 design.

- Six cylinders with different orientations (instead of three in the S1 design) can be seen in Region 5 from side 4A (**fig. 32**). This means that we can visualize defects down to 200 μm in diameter in various orientations.

FIG. 26   PAUT-TFM inspection from side 4A of the S1 aluminum star artifact. The parallel lines represent the longitudinal waves propagating from side 4A.
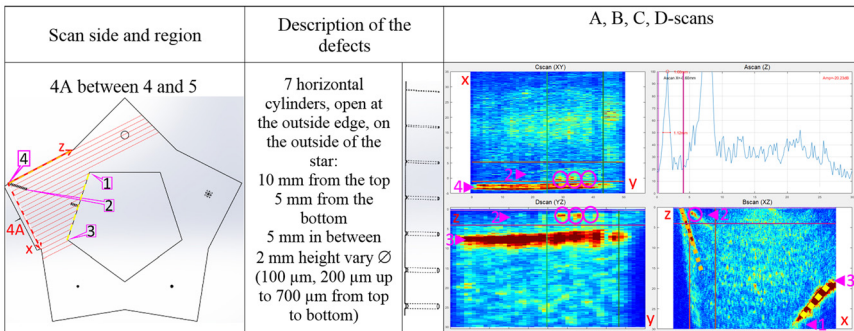

Scan side and region	Description of the defects	A, B, C, D-scans
4A between 4 and 5	7 horizontal cylinders, open at the outside edge, on the outside of the star: 10 mm from the top 5 mm from the bottom 5 mm in between 2 mm height vary ∅ (100 μm, 200 μm up to 700 μm from top to bottom)	

FIG. 27   PAUT-TFM inspection from side 4A of the S1 aluminum star artifact with different scan parameters and scan area than in **Fig. 26**. The parallel lines represent the longitudinal waves propagating from side 4A.
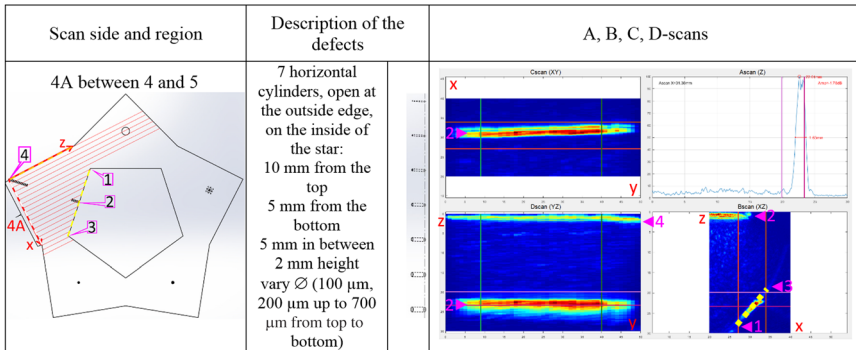
- All vertical cylinders can be seen in Region 4 from the side labeled 3A (**fig. 31**) like in the S1 design, although with increased gain. This means that we can visualize defects down to 100 μm in diameter.
- All spheres (instead of three in the S1 design) can be seen in Region 4 from the side labeled 3A (**fig. 30**). This means that we can visualize defects down to 100 μm in diameter.
- The horizontal cylinders are easier to see when located inside the star artifact (**fig. 28**) than when located outside the star artifact (**fig. 29**). Four of these cylinders are seen in **figure 29**.

Thus, because of its high spatial resolution when used with FMC/TFM, the PAUT method reveals individual defects and even allows rough dimensional

FIG. 28   PAUT-TFM inspection from side 5A of the S2 aluminum star artifact. The parallel lines represent the longitudinal waves propagating from side 5A.
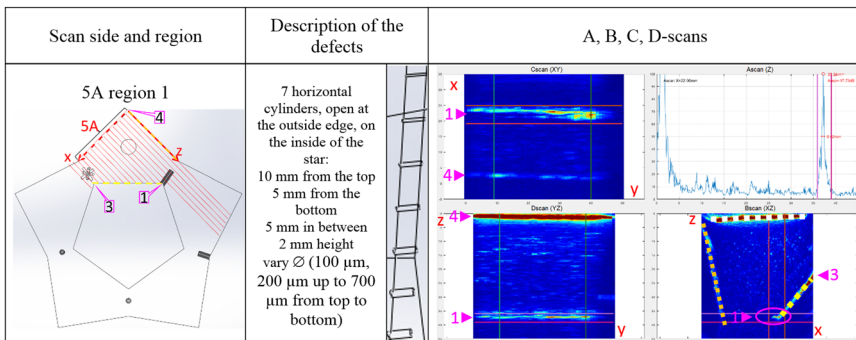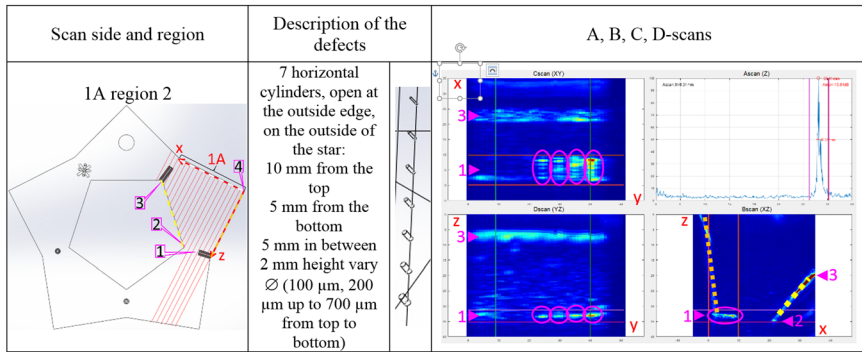

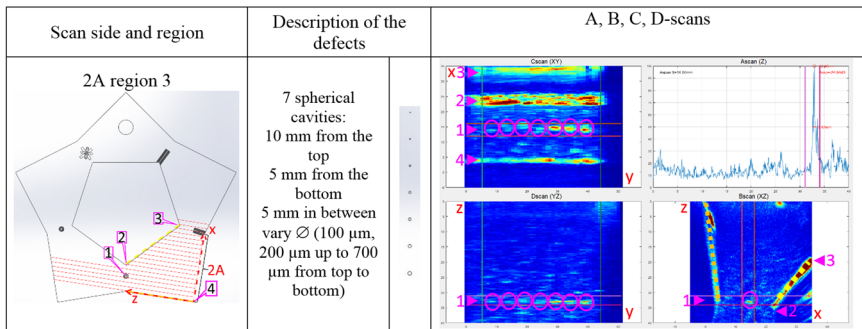Eqr {tki j v'd{ 'CUVO "Kpvl'*cnit'ki j w'tgugtxgf ='Y gf 'Lcp''3; ''37 3: 57'I O V'4244
F qy pmqcf gf Ir tkpvgf 'd{
WU0F GRV'QH'EQO O GTEG'P KUV'*WU0F GRV'QH'EQO O GTEG'P KUV+'r wtuwcpv'vq 'Nkegpug''Ci tggo gpv0P q 'hwtvj gt 'tgrtqf wevkqpu'cwj qtk| gf 0

Scan side and region	Description of the defects	A, B, C, D-scans
1A region 2	7 horizontal cylinders, open at the outside edge, on the outside of the star: 10 mm from the top 5 mm from the bottom 5 mm in between 2 mm height vary Ø (100 µm, 200 µm up to 700 µm from top to bottom)	

Scan side and region	Description of the defects	A, B, C, D-scans
2A region 3	7 spherical cavities: 10 mm from the top 5 mm from the bottom 5 mm in between vary Ø (100 µm, 200 µm up to 700 µm from top to bottom)	

measurements by comparison to reference objects. The interpretation of the images is easier than in CUT but is still not straightforward. Like in CUT, however, the surface roughness did not prevent the part from being tested, and the size of the part was not an obstacle. Apart from the better resolution than in CUT, another real advantage of the PAUT-TFM methods is to be able to perform the static inspection by steering the beam instead of scanning the probe. This is of particular interest for complex shapes that cannot be scanned.

The main benefits of the PAUT–TFM are as follows:

- possibility of inspection without scanning by steering the beam
- less restriction in shape than CUT
- less restriction in size than XCT
- fast scanning (real-time), faster than CUT

FIG. 31 PAUT-TFM inspection from side 3A of the S2 aluminum star artifact. The parallel lines represent the longitudinal waves propagating from side 3A. The two bottom scans correspond to higher digital gains.
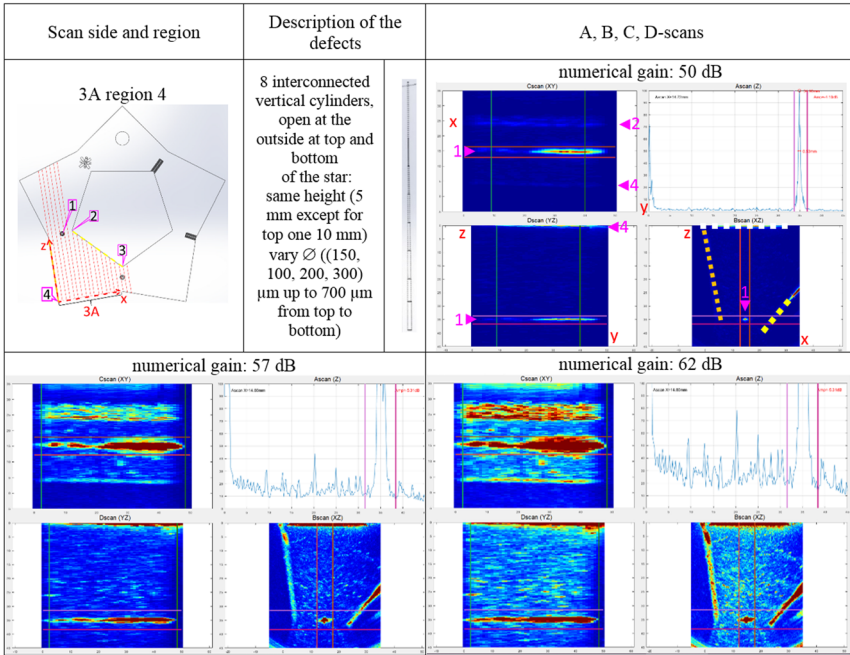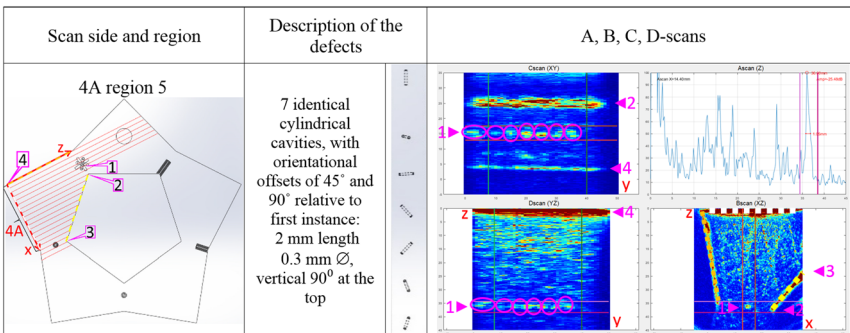

FIG. 32 PAUT-TFM inspection from side 4A of the S2 aluminum star artifact. The parallel lines represent the longitudinal waves propagating from side 4A.

- few roughness restrictions
- ability to identify the type and location of defects in the part
- discretization in size

- rough dimensional measurements by comparison to reference objects

The main drawbacks of the PAUT–TFM are as follows:

- part set-up required
- requires experience
- requires more experience and training than CUT
- more expensive than CUT

SRXCT

Principle of XCT—Tomography is a volumetric imaging method. It consists of probing a test part with electromagnetic waves (e.g., microwaves, terahertz waves, X-ray) or elastic waves (e.g., sound, ultrasound, etc.) at different angular positions of the part, recording the interactions of these waves with the test part for each angle independently, and post-processing these data with a reconstruction algorithm to give a volumetric image. A tomographic device includes a wave source, a sensor that detects the effects of interaction between the waves and the test part (e.g., attenuation, reflection, diffusion, diffraction), and a translation stage with a rotating platform on which the test part is positioned. The most commonly used waves are X-rays, as the short wavelength allows for better spatial resolution of the image. The best-known method of X-ray tomography is XCT.[20–22] In a laboratory XCT system, the X-ray source consists of a high-voltage power supply (usually the voltage (U) ranges between 10 kV and 450 kV) and an X-ray tube made of two electrodes: a filamentary cathode, usually of tungsten, and an anode, which is the target. By applying an electric current (I) to the cathode, electrons are extracted; then, by applying a high potential difference (U) between the anode and the cathode, the electrons are accelerated to collide with the target, focused on a spot on the target, to emit X-rays.

ASTM E1695-95, *Standard Test Method for Measurement of Computed Tomography (CT) System Performance*,[23] describes two factors that affect the quality of an XCT image: geometrical unsharpness, which limits the spatial resolution, and random noise, which limits the contrast sensitivity. Spatial resolution influences the ability to detect small geometrical features in the object, whereas contrast sensitivity influences the ability to detect inhomogeneities in the object. The geometrical unsharpness is linked to the size of the focused spot. This size depends on the required power for the measurement ($P = UI$), which depends on the thickness and density of the test part. The thicker and higher density of the part, the higher the power required, which creates a larger focus spot. An increase in the size of the focus spot induces more geometrical unsharpness. Thus, a larger focus spot results in a decrease in spatial resolution. The random noise is linked to the brilliance of the source, which is proportional to the number of photons produced per second. The higher the brilliance, the lower the random noise. Thus, a higher brilliance results in higher contrast sensitivity.

The produced X-ray beam is polychromatic (multiwavelength), which is not ideal because artifacts (an artificial characteristic on the image) can appear on the image as a result of beam hardening (i.e., loss of the low energies in the source spectrum due to their absorption by the test part).

The beam's shape is commonly conical. This shape causes the magnification (*mag*) of the part on the detector to depend on its position between the source and the detector. The closer the part to the source, the larger its magnification on the detector, which usually is a flat panel composed of a matrix of pixels. This magnification and the size of a pixel of the detector (*pixel$_{size}$*) will define the spatial resolution of the image. Indeed, the spatial resolution is related to the size of the voxel (equivalent in a three-dimensional (3D) image of a pixel) defined as follows:

$$voxel_{size} = pixel_{size}/mag. \qquad (1)$$

The detector records the attenuated intensity of a ray, which is proportional to the thickness and density of material crossed. This enables the ability to acquire two-dimensional (2D) images (i.e., gray-scale images that show the radiation attenuation through the material) called projections. These projections, acquired over 360° around the test part, enable the reconstruction of the image in 3D.

Even though laboratory XCT is the more widespread X-ray tomographic system, tomography is also performed with a SRXCT source.

Principle of SRXCT—Synchrotron radiation is generated by electrons confined in a large loop and accelerated in a magnetic field. Because of the bending of their trajectory, the electrons accelerate or decelerate losing energy and thus produce electromagnetic radiation with a wide polychromatic spectrum from far infrared to hard X-rays. The use of a monochromator allows for the selection of a monochromatic X-ray beam used to perform CT. The detector is generally a scintillator combined with a camera. Otherwise, the SRXCT principle of image acquisition and reconstruction is the same as for laboratory XCT.

Compared with laboratory XCT, in addition to being monochromatic instead of polychromatic, the synchrotron beam is collimated instead of conical, and its brilliance is much higher than laboratory XCT. These are the three main differences between sources from laboratory XCT and synchrotron radiation. These differences are of paramount importance as they enable better spatial resolution, better contrast sensitivity, and fewer artifacts. Indeed, the benefit of a monochromatic beam is that it prevents artifacts on the image. The first benefit of a parallel beam is that the part does not need to be scanned over 360° but simply over 180°. The information acquired is identical from one side to the other. The second benefit is that there is no focused spot that would create geometric unsharpness and thus decrease spatial resolution. The last benefit is that there is no magnification, which means that the spatial resolution is defined only by the pixel size of the detector. The benefit of high brilliance is that it decreases random noise and thus increases contrast sensitivity.

FIG. 33   CAD of the Co-Cr full-star artifact, S2 design, seen from different sides (*R* refer to the Region in the star).
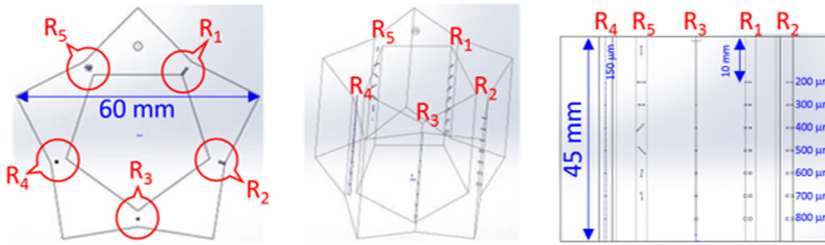

TABLE 7   Experimental parameters used for the XCT inspection using synchrotron of the Co-Cr star

Acquisition Parameters		
Synchrotron radiation source	Energy (keV)	195
Detector	camera	PCO Edge 4.2
	scintillator	LuAg 2000
	image size (pixel)	2048 × 400
	pixel size (μm)	23.3
Acquisition mode (pixel)	Half-acquisition 500	
Exposure time (ms)	15	
Image per projection	20	
Number of projections	5,000	
Number of scans at different vertical locations	10	
Distance between sample and detector (m)	13	

SRXCT of the Co-Cr S2 Star Artifact—An XCT beamline (ID19),[24] from the European Synchrotron Radiation Facility (ESRF) located in Grenoble, France, was used to characterize the S2 design of the Co-Cr star artifact, with the corresponding CAD shown in **figure 33**. The acquisition parameters are given in **table 7** and the different images, processed with the ImageJ software, are displayed in **figure 34** through **figure 38**.

The spatial resolution of the images is indisputably better than the ones from the UT methods. All defects are clearly located and imaged. Inspection of the 3D images also indicated an organic defect (hot tear or crack) at the base of the star (**fig. 39**). The resolution of the images allows for a dimensional comparison with the CAD model (**fig. 40**).

FIG. 34   Star artifact images obtained by SRXCT for Region 1.

Region	CAD description	Defect characteristics		Top view	Face view	Side view
1	7 horizontal cylinders, open at the outside edge, on the inside of the star: 10 mm from the top 5 mm from the bottom 5 mm in between 2 mm height vary ∅, the smaller at the top	∅, µm	200			
			300			
			400			
			500			
			600			
			700			
			800			

FIG. 35   Star artifact images obtained by SRXCT for Region 2.

Region	CAD description	Defect characteristics		Top view	Face view	Side view
2	7 horizontal cylinders, open at the outside edge, on the outside of the star: 10 mm from the top 5 mm from the bottom 5 mm in between 2 mm height vary ∅, the smaller at the top	∅, µm	200			
			300			
			400			
			500			
			600			
			700			
			800			

FIG. 36 Star artifact images obtained by SRXCT for Region 3.

Region	Description	Defect characteristics		Top view	Face view
3	7 spherical cavities: 10 mm from the top 5 mm from the bottom 5 mm in between vary Ø, the smaller at the top	Ø, μm	200		
			300		
			400		
			500		
			600		
			700		
			800		

FIG. 37 Star artifact images obtained by SRXCT for Region 4.

Region	Description	Defect characteristics		Top view	Face view
4	8 interconnected vertical cylinders, open at the outside at top and bottom of the star: 5 mm height except for the smaller 10 mm height vary Ø, the smaller at the top	Ø, μm, and height, mm	Ø=150 μm 10 mm height Ø=200 μm 5 mm height		

FIG. 38   Star artifact images obtained by SRXCT for Region 5.

Region	Description	Defect characteristics		Top view	Face view
5	7 identical cylindrical cavities, with orientational offsets of 45° and 90° relative to first instance: 2 mm height 0.3 mm ∅, Vertical 90° at the top	Angle, degrees, and distance from the top, mm	vertical 90° 3 mm		
			horizontal 0° (radial) 10 mm		
			horizontal 0° (tangential) 15 mm		
			45° 20 mm		
			-45° 25 mm		
			45⁰ 30 mm		
			-45° 35 mm		

The main benefits of XCT are as follows:

- no restriction in shape
- no roughness restrictions
- ability to identify the type and location of defects in the part
- discretization in size
- dimensional measurements by comparison to reference objects

The main drawbacks of XCT are as follows:

- part set-up required
- experience required
- not suitable for high volume and routine quality control
- more expensive than other NDT methods

Conclusion

The paper provides a comparison of NDT methods for typically expected defect sizes and shapes resulting from PBF processes. These methods can be used as the baseline for further analysis, including the application-dependent critical size information.

We have investigated four volumetric NDT methods as potential alternatives to XCT for faster and cheaper characterization for routine control and inspection of additively manufactured metal parts: two whole-body inspection methods using acoustic waves (RAM and PCRT) and two selective inspection methods using

FIG. 39 Organic defect (hot tear or crack) in Region 2.

FIG. 40 Superposition of the CAD and the X-ray scan in Region 2.

ultrasound waves (CUT and PAUT-TFM). The two whole-body inspection methods gave similar results. The parts with defects could be separated from the parts without defects, but the parts with defects could not be sorted based on the number of defects they contained. The results of the two selective inspection methods were significantly

Eqr {tki j v'd{ 'CUVO 'Kpvji''cmi'tki j vu't gugtxgf ±''Y gf 'Lcp''3; '37-3: -57'T O V'4244
F qy pnqcf gf Ir tkpvgf 'd{
WUL0F GRV'QH'EQO O GTEG/P KUV''*WUL0F GRV'QH'EQO O GTEG/P KUV+'r wtuwcpv'vq'Nkegpug'Ci tggo gpv0P q'hwtvj gt 'tgrtqf we vkqpu''cwij qtk| gf 0

different. The CUT method allowed for detection of most of the defects with low-spatial resolution, although defects 5 mm apart could not be discriminated. Further-more, the defects were not detected from every direction; successful results depended on the side inspected. The PAUT-TFM resulted in higher resolution images than CUT, allowing for detection and separation of nearly all defects for any given side inspection. As a comparison, we performed SRXCT, which gave better spatial resolution, better contrast sensitivity, and fewer artifacts than laboratory XCT.

The whole-body inspection methods allowed for only the identification of defective parts, whereas the selective inspection methods allowed for identification of the type of the defect. In applications like routine inspections, it is sufficient to determine that a part is nonconforming to reject it. Then, if localization and size of defects are needed to evaluate the defect criticality and impact on part performance, a secondary evaluation could use a selective inspection method.

Further volumetric NDT methods, such as nonlinear acoustic methods, should be investigated to boost the application of AM in critical sectors and to guarantee the reliability of parts for critical applications.

DISCLAIMER

Certain commercial entities, equipment, or materials may be identified in this docu-ment to describe an experimental procedure or concept adequately. Such identifica-tion is not intended to imply recommendation or endorsement by the National Institute of Standards and Technology, nor is it intended to imply that the entities, materials, or equipment are necessarily the best available for the purpose.

References

1. A. F. Obaton, M.-Q. Lê, V. Prezza, D. Marlot, P. Delvart, P. A. Huskic, S. Senck, E. Mahé, and C. Cayron, "Investigation of New Volumetric Non-Destructive Techniques to Charac-terise Additive Manufacturing Parts," *Welding in the World* 62, no. 5 (2018): 1049–1057, https://doi.org/10.1007/s40194-018-0593-7

2. J. B. Perraud, A. F. Obaton, J. Bou-Sleiman, B. Recur, H. Balacey, F. Darrack, J. P. Guillet, and P. Mounaix, "Terahertz Imaging and Tomography as Efficient Instruments for Testing Polymer Additive Manufacturing Objects," *Applied Optics* 55, no. 13, (2016): 3462–3467, https://doi.org/10.1364/AO.55.003462

3. E. Todorov, R. Spencer, S. Gleeson, M. Jamshidinia, and S. M. Kelly, *America Makes: National Additive Manufacturing Innovation Institute (NAMII) Project 1: Nondestructive Evaluation (NDE) of Complex Metallic Additive Manufactured (AM) Structures*, AFRL-RX-WP-TR-2014-0162, EWI (interim report, Air Force Research Laboratory, Materials and Manufacturing Directorate, Wright-Patterson Air Force Base, Dayton OH, June 2014).

4. B. M. Sharratt, *Non-Destructive Techniques and Technologies for Qualification of Additive Manufactured Parts and Processes: A Literature Review*," DRDC-RDDC-2015-C035 (Defence Research Report, Government of Canada, March 1, 2015) http://web.archive.org/web/20200108154044/https://cradpdf.drdc-rddc.gc.ca/PDFS/unc200/p801800_A1b.pdf

5. *Standard Guide for Resonant Ultrasound Spectroscopy for Defect Detection in Both Metallic and Non-Metallic Parts*, ASTM E2001-18 ASTM International, (West Conshohocken, PA: ASTM International, approved December 6, 2018), https://doi.org/10.1520/E2001-18

6. M. Schiefer and L. Sjoeberg, "Physical Basis of the Resonant Acoustic Method for Flaw Detection," http://web.archive.org/web/20200108153712/http://www.modalshop.com/filelibrary/Physical%20Basis%20of%20the%20Resonant%20Acoustic%20Method%20for%20Flaw.pdf

7. *Standard Practice for Process Compensated Resonance Testing via Swept Sine Input for Metallic and Non-Metallic Parts*, ASTM E2534-15 (West Conshohocken, PA: ASTM International, approved 2015), https://doi.org/10.1520/E2534-15

8. G. Stultz, R. Bono, and M. Schiefer, "Fundamentals of Resonant Acoustic Method NDT," http://www.modalshop.com/techlibrary/Fundamentals%20of%20Resonant%20Acoustic%20Method%20NDT.pdf

9. *Standard Practice for Outlier Screening Using Process Compensated Resonance Testing via Swept Sine Input for Metallic and Non-Metallic Parts*, ASTM E3081-16 (West Conshohocken, PA: ASTM International, approved December 1, 2016), https://doi.org/10.1520/E3081-16

10. W. H. Woodall, R. Koudelik, K.-L. Tsui, S. Bum Kim, Z. G. Stoumbos, and C. P. A. Carvounis, "A Review and Analysis of the Mahalanobis—Taguchi System," *Technometrics* 45, no. 1 (2003): 1–15, https://doi.org/10.1198/004017002188618626

11. E. Biedermann, J. Heffernan, A. Mayes, G. Gatewood, L. Jauriqui, B. Goodlet, T. Pollock, C. Torbet, J. C. Aldrin, and S. Mazdiyasni, "Process Compensated Resonance Testing Modeling for Damage Evolution and Uncertainty Quantification," in *AIP Conference Proceedings* 1806, 090005 (New York: American Institute of Physics, 2017), 090005-1–090005-10, https://doi.org/10.1063/1.4974649

12. *Standard Practice for Detection and Evaluation of Discontinuities by the Immersed Pulse-Echo Ultrasonic Method Using Longitudinal Waves*, ASTM E1001-16 (West Conshohocken, PA: ASTM International, approved December 1, 2016), https://doi.org/10.1520/E1001-16

13. Olympus, "Ultrasonic Transducers Technical Notes," 2006, http://web.archive.org/save/https://mbi-ctac.sites.medinfo.ufl.edu/files/2017/02/ultrasound-basics.pdf

14. Olympus, "Ultrasonic Flaw Detection Tutorial," http://web.archive.org/web/20200108154230/https://www.olympus-ims.com/en/ndt-tutorials/flaw-detection/

15. Olympus, "Phased Array Tutorial," http://web.archive.org/web/20200108155804/https://www.olympus-ims.com/en/ndt-tutorials/phased-array/

16. M. Karaman, P.-C. Li, and M. O'Donnell, "Synthetic Aperture Imaging for Small Scale Systems," *IEEE Transactions on Ultrasonics, Ferroelectrics and Frequency Control*, 42, no. 3 (1995): 429–442, http://doi.org/10.1109/58.384453

17. C. Holmes, B. W. Drinkwater, and P. D. Wilcox, "Post-Processing of the Full Matrix of Ultrasonic Transmit-Receive Array Data for Non-Destructive Evaluation," *NDT&E International* 38, no. 8 (2005): 701–711, http://doi.org/10.1016/j.ndteint.2005.04.002

18. R. Spencer, R. Sunderman, and E. Todorov, "FMC/TFM Experimental Comparisons," in *44th Annual Review of Progress in Quantitative Nondestructive Evaluation*, Vol. 37 (New York: American Physics Institute, 2018), 020015-1–020015-5, https://doi.org/10.1063/1.5031512

19. E. Carcreff, G. Dao, and D. Braconnier, "Total Focusing Method for Flaw Characterization in Homogeneous Media" (paper presentation, Fourth International Symposium on Non-destructive Characterization of Materials, Marina Del Rey, FL, June 22–26, 2015), https://www.researchgate.net/profile/Ewen_Carcreff/publication/282654039_Total_focusing_method_imaging_for_flaw_characterization_in_homogeneous_media/links/56162ac70 8ae4ce3cc65a588/Total-focusing-method-imaging-for-flaw-characterization-in-homo-geneous-media.pdf

20. A.-F. Obaton, J. Fain, M. Djemaï, D. Meinel, F. Léonard, E. Mahé, B. Lécuelle, J-.J. Fouchet, and G. Bruno, "in vivo XCT Bone Characterization of Lattice Structured Implants Fabri-cated by Additive Manufacturing: A Case Report," *Heliyon* 3, no. 8 (2017): E00374, http://doi.org/10.1016/j.heliyon.2017.e00374

21. P. Hermanek and S. Carmignato, "Reference Object for Evaluating the Accuracy of Porosity Measurements by X-Ray Computed Tomography," *Case Studies in Nondestruc-tive Testing and Evaluation* 6, Pt. B (2016): 122–127, http://doi.org/10.1016/j.csndt.2016.05.003

22. F. H. Kim, S. P. Moylan, E. J. Garboczi, and J. A. Slotwinski, "Investigation of Pore Struc-ture in Cobalt Chrome Additively Manufactured Parts Using X-Ray Computed Tomogra-phy and Three-Dimensional Image Analysis," *Additive Manufacturing* 17 (2017): 23–38, http://doi.org/10.1016/j.addma.2017.06.011

23. *Standard Test Method for Measurement of Computed Tomography (CT) System Perfor-mance*, ASTM E1695-95(2013) (West Conshohocken, PA: ASTM International, approved June 1, 2013), http://doi.org/10.1520/E1695-95R13

24. *ID19—Microtomography Beamline* (Grenoble, France: European Synchrotron Radiation Facility), http://web.archive.org/web/20200108161206/https://www.esrf.eu/home/UsersAndScience/Experiments/StructMaterials/ID19.html